Resonant amplification of MHD waves in realistic subsolar magnetopause configurations

J. de Keyser, M. Roth, F. Reberac, L. Rezeau, G. Belmont

JOURNAL OF GEOPHYSICAL RESEARCH, VOL. 104, NO. A2, PAGES 2399–2409, FEBRUARY 1, 1999

Resonant amplification of MHD waves in realistic subsolar magnetopause configurations

J. De Keyser and M. Roth

Belgian Institute for Space Aeronomy, Brussels

F. Reberac, L. Rezeau, and G. Belmont

Centre d'Étude des Environnements Terrestre et Planétaires, Vélizy, France

Abstract. Broadband ULF fluctuations are routinely observed throughout the magnetosheath; the fluctuation level peaks at the magnetopause and becomes very small in the magnetosphere. The present paper analyzes the propagation of magnetosheath waves and the transport of energy at the subsolar magnetopause by means of a linear perturbation analysis in the limit of the MHD approximation. We examine realistic equilibrium magnetopause configurations with a cold and dense magnetosheath and a hot, tenuous magnetosphere, possibly including a trapped magnetopause population. The effects of magnetic field rotation are examined. Resonant amplification of monochromatic magnetosonic waves at the magnetopause is found to occur under various conditions. For a given frequency, several field lines inside the magnetopause layer can resonate simultaneously.

1. Introduction

The dayside magnetopause interfaces the shocked solar wind in the magnetosheath (relatively cold and dense) and the hot, tenuous magnetospheric plasma. The magnetopause layer carries the diamagnetic current that is associated with the magnetic field rotation from its magnetosheath orientation (related to the interplanetary magnetic field) to the northward magnetospheric dipole field. The overall structure of the magnetospheric boundary can be understood in terms of equilibrium models, which assume the magnetopause to be locally in a tangential or rotational discontinuity state [e.g., *Su and Sonnerup*, 1968; *Lee and Kan*, 1979; *Paschmann et al.*, 1979; *De Keyser and Roth*, 1997]. It is, however, generally accepted that time-dependent phenomena are important, especially for mass and energy transport across the interface. Such phenomena include flux transfer events, impulsive penetration of plasma, and the Kelvin-Helmholtz instability. One of the open problems is the question of how the presence of ultralow-frequency (ULF) fluctuations influences the transport of plasma and energy across the magnetopause [*LaBelle and Treumann*, 1988].

ULF fluctuations are known to be present continuously in the magnetosheath, the magnetopause, and the low-latitude boundary layer; the fluctuation level peaks inside the magnetopause and drops to a very low value in the magnetosphere [*LaBelle and Treumann*, 1988; *Rezeau et al.*, 1989, 1993; *Song et al.*, 1993]. The magnetosheath fluctuations can be associated with the bow shock geometry, and they have been shown to have consequences on the internal magnetospheric Pc3–Pc4 pulsations [*Engebretson et al.*, 1991]. The strong fluctuation level at the magnetopause was first supposed to be due to a local instability of the boundary itself, but *Belmont et al.* [1995] suggested that it could also be a consequence of the amplification of the magnetosheath fluctuations that propagate downstream. This "resonant amplification" is a process invoked in other contexts as well, in particular for the generation of magnetospheric pulsations [*Southwood*, 1974; *Zhu and Kivelson*, 1989] and for heating of the solar corona [see *Hollweg*, 1997, and references therein]. It is worth noticing that MHD wave propagation can give rise to two different kinds of resonances: (1) "field line resonances", when the length of a magnetic field line is a multiple of the parallel wavelength (like in "cavity modes"), and (2) "mode resonances", when the wavelength in the direction of the inhomogeneity of the medium locally goes down to zero, which can occur for Alfvén and slow modes. It is this phenomenon that is supposed to give rise to the fluctuation level enhancement at the magnetopause. The *Belmont et al.* [1995] paper was limited by the hypothesis of a cold plasma and a unidirectional magnetic field, so that Alfvén velocity variations are produced only by changes in plasma density. The present paper extends the analysis by considering tangential discontinuity configurations that include finite temperature effects and that allow density, temperature, magnetic field intensity and orientation to change across the magnetopause.

The particular merit of this paper lies in the study of resonant amplification in realistic subsolar magnetopause configurations, including magnetic shear effects. The validity of the present study remains, however, limited to the case of frequencies negligible with respect to the proton gyrofre-

Paper number 1998JA900060.
0148-0227/99/1998JA900060$09.00

quency, since it is performed under MHD conditions. As the broadband fluctuation spectrum extends beyond the proton gyrofrequency, it can explain only part of the fluctuation enhancement. Nevertheless, it corroborates the scenario that magnetosheath ULF fluctuations can propagate downstream and cause an increased fluctuation level at the magnetopause by resonant amplification.

2. Ideal MHD Perturbation Analysis

We take the subsolar magnetopause to be planar, with the x axis being the Earth–Sun line ($x < 0$ corresponds to the magnetosphere). We will consider small-amplitude periodic perturbations of an ideal MHD magnetopause equilibrium configuration, which represent the ULF fluctuations. We denote the mass density by ρ, the bulk velocity by $\boldsymbol{v}$, the magnetic field by $\boldsymbol{B}$, and the thermal pressure by p.

2.1. Equilibrium Configuration

The equilibrium configuration is assumed to be of the tangential discontinuity type without tangential plasma flow, that is, $B_x^{(0)} \equiv 0$, $\boldsymbol{v}^{(0)} \equiv \boldsymbol{0}$. Let the magnetospheric field $B^*_{\mathrm{msph}} = B^{(0)}(-\infty)$ and the magnetospheric and magnetosheath mass densities and temperatures ρ^*_{msph}, ρ^*_{msh}, T^*_{msph}, T^*_{msh} be given. The ion mass is denoted by m. We then adopt the following equilibrium profiles:

$$\begin{aligned}
\rho^{(0)}_{\mathrm{msph}}(x) &= \rho^*_{\mathrm{msph}}\mathcal{G}(x/D),\\
\rho^{(0)}_{\mathrm{msh}}(x) &= \rho^*_{\mathrm{msh}}\mathcal{G}(-x/D),\\
\rho^{(0)}(x) &= \rho^{(0)}_{\mathrm{msph}}(x) + \rho^{(0)}_{\mathrm{msh}}(x),\\
T^{(0)}(x) &= [T^*_{\mathrm{msph}}\rho^{(0)}_{\mathrm{msph}}(x) + T^*_{\mathrm{msh}}\rho^{(0)}_{\mathrm{msh}}(x)]/\rho^{(0)}(x),\\
p^{(0)}_{\mathrm{th}}(x) &= k_B\rho^{(0)}T^{(0)}(x)/m,
\end{aligned}$$

where the transition function $\mathcal{G}(x/D) = \frac{1}{2}\,\mathrm{erfc}\,(x/D)$ allows a smooth density variation with half-width D (where erfc denotes the complementary error function); this choice is inspired by analytic tangential discontinuity models [*Roth et al.*, 1996]. We prescribe a smooth rotation of the magnetic field through an angle θ^* in the same region:

$$\theta^{(0)}(x) = \tfrac{\theta^*}{2}\,\mathrm{erf}\,(x/D)$$

(with erf denoting the error function). We adopt the numerical values $\rho^*_{\mathrm{msph}}/m = 1\ \mathrm{cm}^{-3}$, $\rho^*_{\mathrm{msh}}/m = 20\ \mathrm{cm}^{-3}$, $T^*_{\mathrm{msph}} = 20 \times 10^6$ K, $T^*_{\mathrm{msh}} = 4 \times 10^6$ K, $B_{\mathrm{msph}} = 65$ nT, and a magnetopause half-thickness $D = 300$ km [*Berchem and Russell*, 1982]. The magnetic field profile is then determined from the pressure balance condition, with $B_{\mathrm{msh}} = 46$ nT. Different rotation angles θ^* will be considered. This equilibrium configuration, shown in Figure 1, is more realistic than the cold plasma, zero magnetic shear case studied by *Belmont et al.* [1995]. We find Alfvén speeds $v_{A,\mathrm{msh}} = 225\ \mathrm{km\,s^{-1}} < v_{A,\mathrm{msph}} = 1420\ \mathrm{km\,s^{-1}}$ and sound speeds $c_{s,\mathrm{msh}} = 235\ \mathrm{km\,s^{-1}} < c_{s,\mathrm{msph}} = 525\ \mathrm{km\,s^{-1}}$, which means $\beta_{\mathrm{msph}} = 0.13$ and $\beta_{\mathrm{msh}} = 1.09$ ($\beta = c_s^2/v_A^2$).

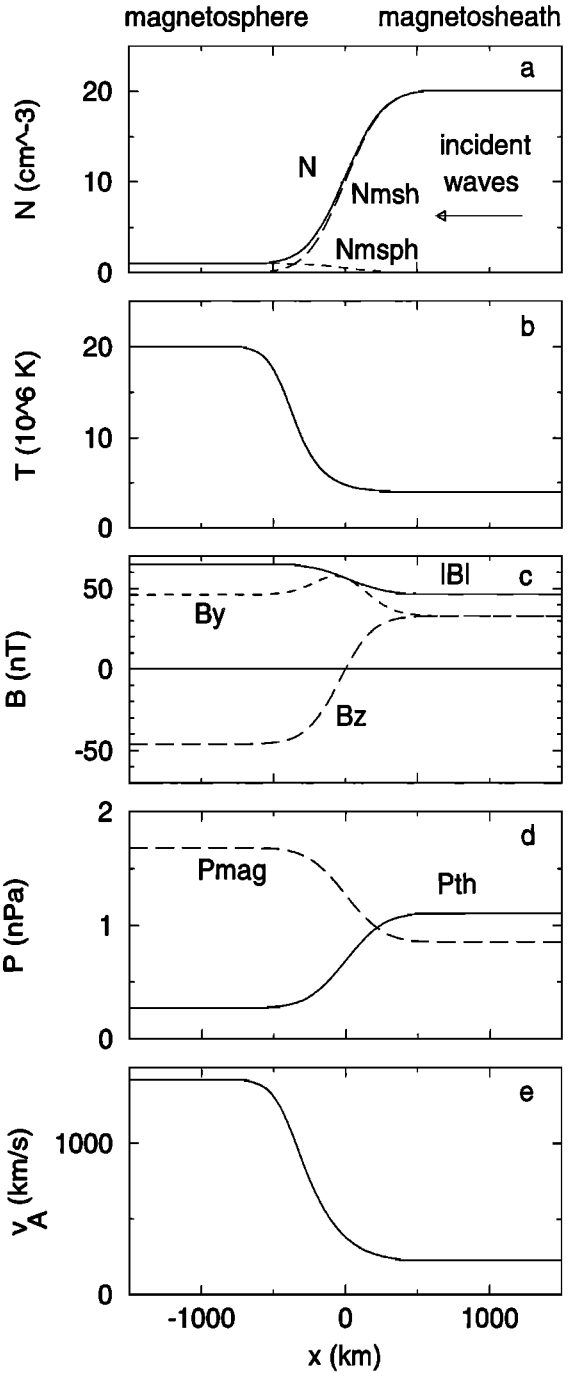

Figure 1. Subsolar magnetopause equilibrium adopted in this paper (for 90° magnetic shear). The x axis is the Earth–Sun line; the y, z plane is parallel to the locally planar magnetopause. The magnetosphere is to the left, the magnetosheath to the right of the magnetopause. The y axis is the bisector of the magnetospheric and magnetosheath magnetic field directions $\boldsymbol{B}^{(0)}_{\mathrm{msph}}$ and $\boldsymbol{B}^{(0)}_{\mathrm{msh}}$. (a) Magnetosheath, magnetospheric, and total number density; (b) temperature; (c) magnetic field; (d) magnetic and thermal pressure; and (e) Alfvén velocity.

2.2. First-Order Perturbation

Consider perturbed quantities

$$q(\boldsymbol{r}, t) = q^{(0)}(x) + \hat{q}^{(1)}(x)e^{i(\boldsymbol{k}_t\cdot\boldsymbol{r}-\omega t)},$$

where $\boldsymbol{r} = [x, y, z]$ is the position vector of a plasma element, $\omega = 2\pi\nu$ is the angular frequency ($\nu = 0.5$ Hz is used in the examples), and $\boldsymbol{k}_t = [0, k_y, k_z]$ is the tangential wave vector. The linearization of the ideal MHD equations is discussed in the Appendix. The normal plasma displacement $\xi_x(x)$ and the total pressure perturbation $\tau(x)$ are both continuous, even across MHD discontinuities. The perturbation can be computed once the quantity $g = \tau/\xi_x = \hat{\tau}/\hat{\xi}_x$ is known; the linearized MHD equation for g is [*Belmont et al.*, 1995]

$$\frac{\partial g}{\partial x} = \frac{iK_x}{G}(G^2 - g^2), \tag{1}$$

where

$$K_x^2 = \frac{\omega^2}{v_A^2 + c_s^2\Omega^2/\omega^2} - k_t^2,$$

$$G = \frac{\rho^{(0)}\Omega^2}{iK_x},$$

$$\Omega^2 = \omega^2 - (\boldsymbol{k}\cdot\boldsymbol{v}_A)^2.$$

Here $\boldsymbol{v}_A = \boldsymbol{B}^{(0)}/(\mu_0\rho^{(0)})^{1/2}$ is the local Alfvén speed. We have solved (1) by complex numerical integration. We impose as boundary condition that there must be a linearly polarized, earthward propagating wave on the magnetospheric side ($g(-\infty) = \pm G$ as will be shown later; the sign is chosen such that the amplitude of the wave remains bounded). In the Appendix we show how the perturbed magnetic field, velocity, density, pressure, and electric field are computed, as well as the time-averaged energy flux.

3. Magnetosonic Wave Propagation

We first study the propagation of monochromatic magnetosonic ideal MHD waves in the uniform magnetosheath and magnetospheric regions. The only MHD waves whose propagation velocity can have a nonvanishing component along the Sun–Earth line are the fast and slow magnetosonic modes. Uniform plasma parameters and a constant magnetic field imply constant v_A, c_s, Ω, K_x, and G. It can be shown that bounded solutions for $\xi_x(x)$ and $\tau(x)$ exist only when $K_x^2 \geq 0$. The simplest solution then is a linearly polarized wave with $k_x = \pm K_x$, corresponding to a magnetosonic wave propagating to the left or to the right, in which case g is constant. Equation (1) then implies that $g = \pm G$, that is, g is purely imaginary: ξ_x and τ are 90° out of phase.

Let $k_A = \omega/v_A$. The angle between $\boldsymbol{k}_t$ and $\boldsymbol{B}^{(0)}$ is denoted by θ. The propagation condition $K_x^2 \geq 0$ is equivalent to

$$k_t^2/k_A^2 \leq \frac{1}{1 + \beta(1 - (k_t^2/k_A^2)\cos^2\theta)}. \tag{2}$$

For $\beta = 0$ the denominator never becomes zero; the wave propagates if $k_t < k_A$, that is, if the propagation domain in the wave vector plane is circular. When $\beta > 0$, the denominator on the right-hand side is zero when $|k_\parallel| = |k_t\cos\theta| = k_S = \omega\sqrt{1+\beta}/c_s$, which corresponds to a resonance of the slow mode. Consider the case $|k_\parallel| < k_S$: the right-hand side in (2) then is positive, and the condition is

$$\beta\cos^2\theta\left(\frac{k_t}{k_A}\right)^4 - (1+\beta)\left(\frac{k_t}{k_A}\right)^2 + 1 \geq 0. \tag{3}$$

The zeros of this biquadratic expression are

$$k_\pm^2 = k_A^2\frac{(1+\beta) \pm \sqrt{(1+\beta)^2 - 4\beta\cos^2\theta}}{2\beta\cos^2\theta}. \tag{4}$$

For each angle θ there exist two zeros $k_\pm$ (with $k_- < k_+$; we allow only positive wave numbers). The case $k_- = k_+$ occurs for $\beta = 1$ and $|\cos\theta| = 1$. It is easy to check that magnetosonic waves can propagate when $0 \leq k_t \leq k_-$ or $k_+ \leq k_t < k_S/\cos\theta$ (note that always $k_+ < k_S/\cos\theta$). A similar analysis shows that there are only evanescent solutions when $|k_\parallel| > k_S$. The biquadratic equation is degenerate for $\theta = \pm\pi/2$; the propagation condition then becomes $0 \leq k_t \leq k_A/\sqrt{1+\beta}$. For $\theta = 0$ and $\beta > 1$ the values k_- and k_+ are $k_A/\sqrt{\beta}$ and k_A; when $\beta < 1$, one has

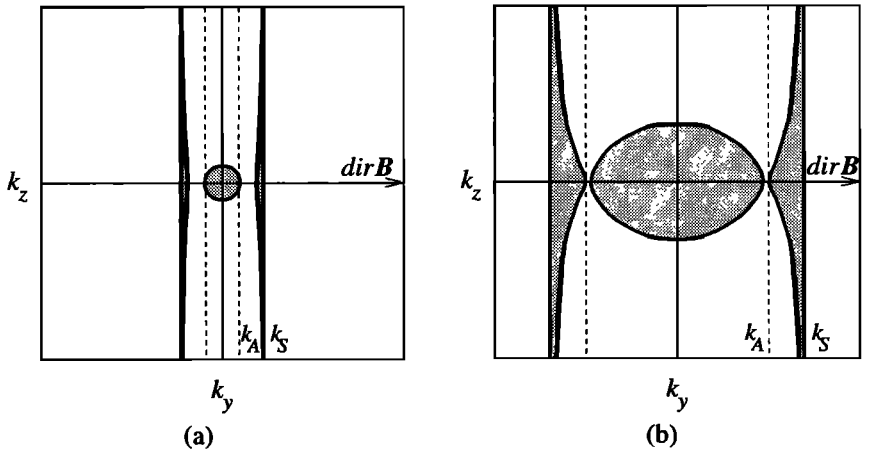

Figure 2. Projection of the dispersion relation on the k_y, k_z plane (tangential to the magnetopause) showing the magnetosonic wave propagation domain (shaded regions) and the Alfvén and slow-wave resonance conditions ($k_\parallel = k_A$ and $k_\parallel = k_S$) (a) in the magnetosphere ($\beta = 0.13$) and (b) in the magnetosheath ($\beta = 1.09$). Both figures are made on the same scale. The y axis points along $\boldsymbol{B}^{(0)}$.

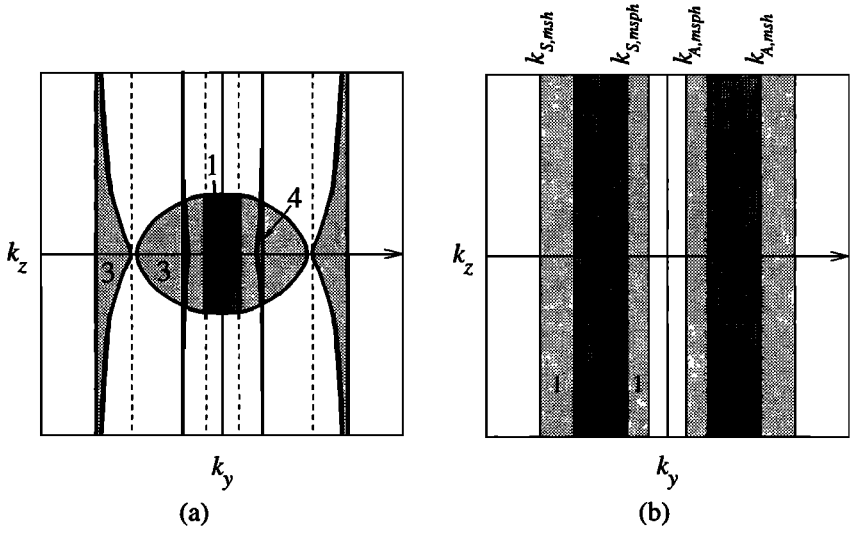

Figure 3. Projection of the dispersion relation on the k_y, k_z plane for the zero magnetic shear magnetopause. The y axis points along $\boldsymbol{B}^{(0)}$. (a) Superposition of the dispersion relations for magnetosphere and magnetosheath (see Figures 2a and 2b). There are four distinct solution classes (the regions where each of these classes occurs are shaded differently): class 1, partial reflection and partial transmission; class 2, complete reflection; class 3, partial reflection and partial absorption; and class 4, partial reflection, partial transmission, and partial absorption. (b) Number of resonance points; light shading indicates a single resonance, darker shading indicates simultaneous resonance at two points inside the magnetopause.

$k_- = k_A$ and $k_+ = k_A/\sqrt{\beta}$. Figure 2 shows the wave vector diagram, that is, the dispersion relation projected onto the k_y, k_z plane, for the magnetosphere and magnetosheath parameters chosen earlier. The shaded regions correspond to wave vectors for which magnetosonic waves of a given frequency can propagate (the diagram scales with k_A or, equivalently, ω). The magnetic field vector is oriented along the k_y axis. For the magnetospheric case (Figure 2a) β is small, so that $k_- \ll k_+$. In the magnetosheath (Figure 2b), however, β is close to unity, and k_- and k_+ nearly coincide for $\theta = 0$ or π.

4. Resonant Amplification

The nature of the solution of (1) depends on the boundedness of the coefficient $iK_x/G = -K_x^2/\rho^{(0)}\Omega^2$ inside the magnetopause. If it is unbounded at a certain point inside the magnetopause, $G = 0$ at such a singularity, that is, $\Omega^2 = 0$ or K_x^2 is infinite:

$$\omega = |k_\parallel| v_A, \tag{5}$$

$$\omega = \frac{|k_\parallel| c_s}{\sqrt{1+\beta}}. \tag{6}$$

These two conditions correspond to the Alfvén and slow-mode waves, respectively. At each point where one of both conditions is satisfied, the x variations characterizing the involved mode occur on a scale that becomes infinitely short, leading to the divergence for some components (unboundedness of $|\partial g/\partial x|$). This phenomenon is called "resonant amplification". Equation (1) can then no longer be solved. The nature of this singularity is discussed by *Southwood* [1974]. In order to avoid the occurrence of a true singularity (which is due to the oversimplicity of the model) in the numerical computations, we have used the technique advocated by *Belmont et al.* [1995]: we add a small complex component to k_t. Essentially, this means that we use perturbations that have a low-frequency modulation tangential to the magnetopause surface. *Southwood* [1974] and *Hollweg* [1997] avoid the singularity by explicitly including an energy absorption process in the model.

4.1. No Magnetic Shear

We first consider the situation of a unidirectional magnetic field $\boldsymbol{B}^{(0)}$ parallel to the y axis. At the magnetopause, it is generally found that $k_{A,\mathrm{msph}} < k_{A,\mathrm{msh}}$. Therefore a magnetosonic wave of magnetosheath origin can propagate earthward toward the magnetopause, but it is not necessarily transmitted across the magnetopause since it may not be able to propagate into the magnetosphere. For a given vector $\boldsymbol{k}_t$, either zero or one resonant amplification point can be found from (5), at least if k_A (or v_A) varies monotonously across the magnetopause. If it exists, the resonant point x^* satisfies $k_A(x^*) = k_\parallel$. A similar result can be obtained from (6). Therefore resonant amplification occurs when (5) or (6) are fulfilled, which implies

$$k_{A,\mathrm{msph}} < |k_\parallel| < k_{A,\mathrm{msh}} \text{ or}$$
$$k_{S,\mathrm{msph}} < |k_\parallel| < k_{S,\mathrm{msh}}.$$

When both intervals for $|k_\parallel|$ overlap, there can be simultaneous resonance at up to two points inside the magnetopause.

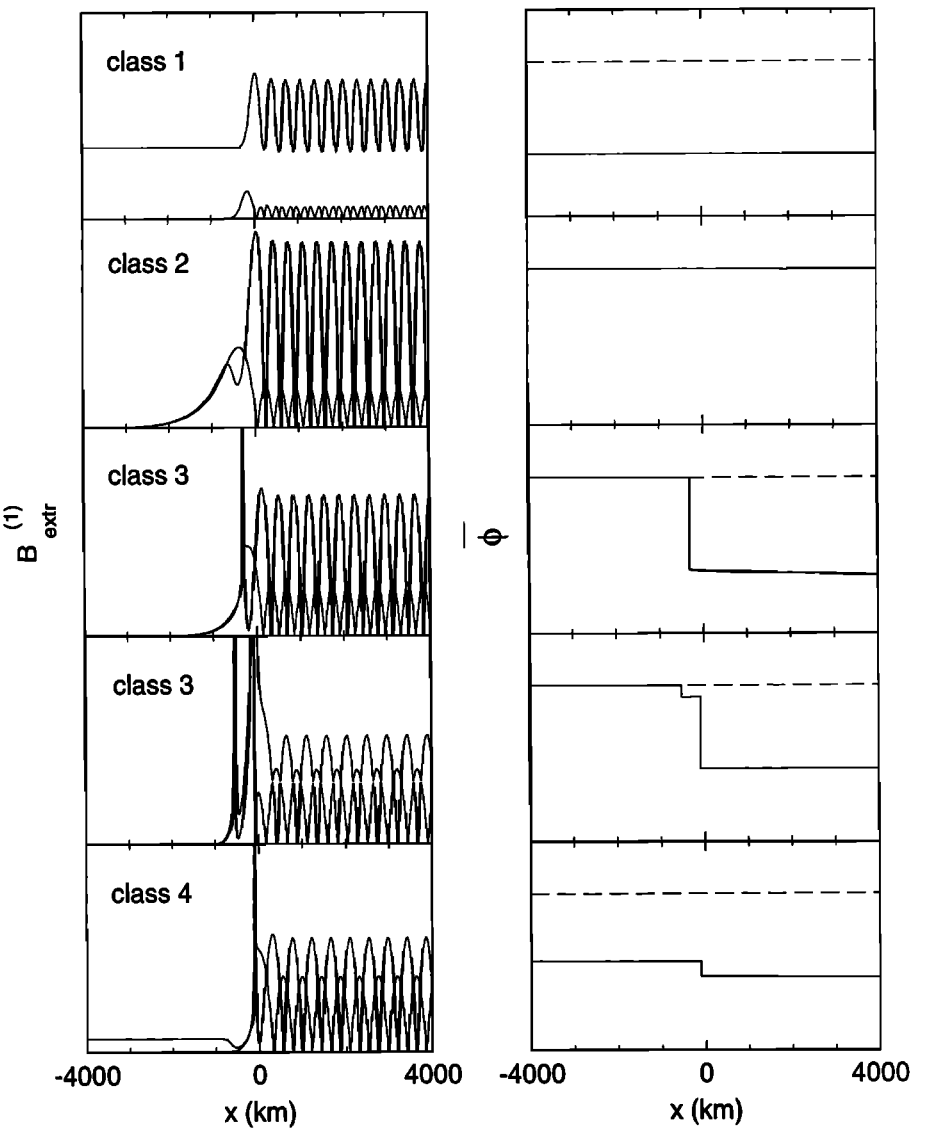

Figure 4. Representative solutions for the zero magnetic shear magnetopause in the warm plasma case. The figures plot the maximum and minimum values of the modulus of (left) $\boldsymbol{B}^{(1)}$ (in arbitrary units) and (right) the time-averaged energy flux $\bar{\phi}$ (in arbitrary units; zero flux corresponds to the dashed horizontal line) as a function of the distance to the center of the magnetopause (in km). The magnetosphere is to the left and the magnetosheath is to the right of the magnetopause. Class 1: a nonvanishing perturbation intensity in the magnetosphere indicates transmission, while the energy flux remains constant as the incident flux equals the transmitted flux plus the reflected one. In the reference frame adopted here, a negative flux $\bar{\phi} < 0$ indicates energy transfer from the magnetosheath to the magnetosphere. Class 2: the wave does not penetrate into the magnetosphere and is completely reflected, resulting in a net zero energy flux. Class 3: similar to class 2 but now resonant amplification (infinite wave amplitude) occurs at one or two points inside the magnetopause; resonant absorption implies a jump in the energy flux profile. Class 4: reflection, transmission, and resonant amplification occur simultaneously; again, ϕ is discontinuous at the resonant points.

In the cold plasma case the second condition is never met; there is at most one resonant point [*Belmont et al.*, 1995]. Figure 3a shows the wave vector diagram. The solid lines demarcate the propagation domains of magnetosonic waves in the magnetosheath and the magnetosphere, respectively. The dashed lines demarcate the resonant amplification regions. *Belmont et al.* [1995, Figure 2] identified three solution classes in the cold plasma limit: class 1, the magnetosheath wave propagates through the magnetopause and continues earthward in the magnetosphere; class 2, the magnetosheath wave is not transmitted; and class 3, the magnetosheath wave is not transmitted, but resonant amplification does occur. In the warm plasma case there is an additional class: class 4, waves that are both transmitted and resonantly amplified. Figure 3b counts the number of resonance points in the wave vector plane. Some representative solutions of

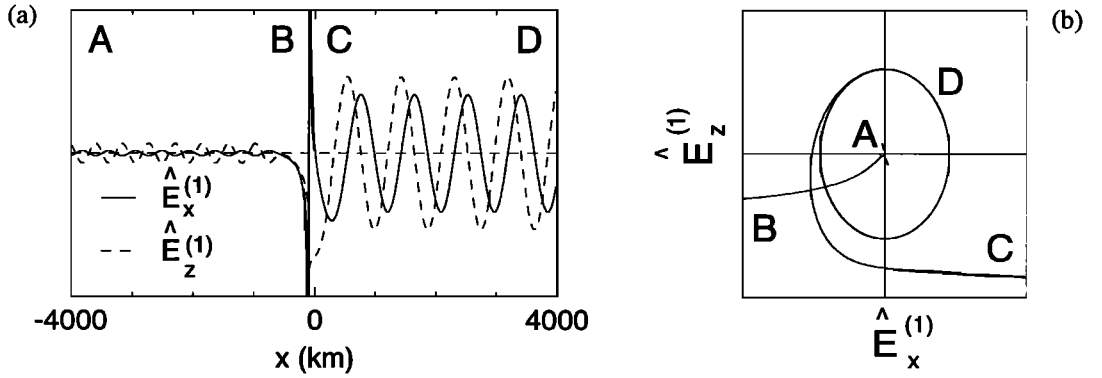

Figure 5. Electric field polarization for the class 4 solution of Figure 4. (a) Plot of the electric field components $\hat{E}_x^{(1)}$ and $\hat{E}_z^{(1)}$ (in arbitrary units) along the Earth–Sun line ($\hat{E}_y^{(1)} \equiv 0$ as $\boldsymbol{B}^{(0)}$ parallel to y). (b) $\hat{E}_x^{(1)}$,$\hat{E}_z^{(1)}$ hodogram, showing the linear polarization in the magnetosphere (labeled A) and the elliptic polarization in the magnetosheath (labeled D), while $\hat{E}^{(1)}$ is unbounded at the resonance point (labels B and C immediately left and right of the resonance point, respectively).

each class are shown in Figure 4. The figure shows for each solution the values between which the magnetic field perturbation varies at each position along the Earth–Sun line, as well as the corresponding energy flux profile. Resonant points are easily identified since the perturbation becomes unbounded there (classes 3 and 4). Waves penetrating the magnetosphere are characterized by a nonvanishing amplitude in the magnetosphere (classes 1 and 4). As shown in the Appendix, the time-averaged energy flux $\bar{\phi}$ along the Earth–Sun line must be constant for ideal MHD and real $\boldsymbol{k}_t$, except at singular points. A small departure from these ideal conditions implies energy flux changes only at points where the gradients are large, that is, at the singular points. In the present calculation, no dissipative terms are included, but an imaginary part has been added to the tangential wave vector $\boldsymbol{k}_t$. This means that the energy flux is not actually absorbed, but only diverted into the tangential plane. Class 1 solutions, which have no singular points, are therefore characterized by a constant earthward flux $\bar{\phi} < 0$; the energy flux associated with the magnetospheric wave equals the flux of the incident minus the reflected magnetosheath waves. In class 2 solutions, all the incident flux is reflected back, so that $\bar{\phi} = 0$. Class 3 and 4 solutions possess singular points (the resonant points) where $\bar{\phi}$ can be discontinuous. We have checked that the jump values are independent of the size of the imaginary part of the wave vector, as long as the imaginary part is small enough so that the resonance peak is narrower than the magnetopause gradient scale. The numerical integration step should of course be even smaller so as to resolve the resonance peak.

Figure 5 plots the electric field perturbation $\hat{\boldsymbol{E}}^{(1)}$ for the class 4 solution shown in Figure 4. For a unidirectional $\boldsymbol{B}^{(0)}$ along y, one has $\hat{E}_y^{(1)} \equiv 0$. Earthward of the magnetopause (labeled A in the figure) the electric field polarization is linear (by choice of boundary condition). At the resonance point (B, C), $\hat{E}^{(1)}$ becomes unbounded. In the magnetosheath (D) the electric field is the superposition of the fields associated with the incident and reflected waves, resulting in an elliptical polarization. This is consistent with the result of *Southwood* [1974] that the polarization sense can change only at extrema of the electric field magnitude, the only extremum here being at the resonance point. Note that this result would imply subsequent polarization sense changes in the class 3 solutions with multiple resonance points. However, with the magnetopause thickness adopted here, the distance between the resonance points spans only part of a wavelength, so that the polarization sense cannot clearly be established there.

4.2. Nonzero Magnetic Shear

The presence of magnetic field rotation complicates the resonant amplification conditions. In the discussion below we choose the y axis to be the bisector of $\boldsymbol{B}^{(0)}_{\text{msph}}$ and $\boldsymbol{B}^{(0)}_{\text{msh}}$, and we take $k_{A,\text{msph}} < k_{A,\text{msh}}$ and $k_{S,\text{msph}} < k_{S,\text{msh}}$ (the situation at the magnetopause). Figure 6 shows the hodogram of $\boldsymbol{k}_A = k_A \boldsymbol{B}^{(0)}/B^{(0)}$ for magnetopause configurations with or without magnetic shear. Figure 6a is made for a unidirectional magnetic field along y; the $\boldsymbol{k}_A(x)$ hodogram then is a straight line. As discussed earlier, and as illustrated graphically, there can be at most one resonant point when $k_A(x)$ is monotonous. A similar construction can be made using the hodogram for $\boldsymbol{k}_S = k_S \boldsymbol{B}^{(0)}/B^{(0)}$, possibly leading to a second resonant point. Figure 6b shows the $\boldsymbol{k}_A$ hodogram for the case of nonzero magnetic shear, with monotonous $k_A(x)$ and monotonous magnetic field rotation over 90°. The graphical construction shows that resonant amplification according to (5) can occur simultaneously at two different points inside the magnetopause for a given wave vector. Resonance is obtained at those points where $k_\parallel = k_A(x)$, that is, at those points where the projection of $\boldsymbol{k}$ on the direction of $\boldsymbol{B}^{(0)}(x)$ coincides with $\boldsymbol{k}_A(x)$.

The wave vector diagram is given in Figure 7a; it is obtained by superposing the propagation domains for magne-

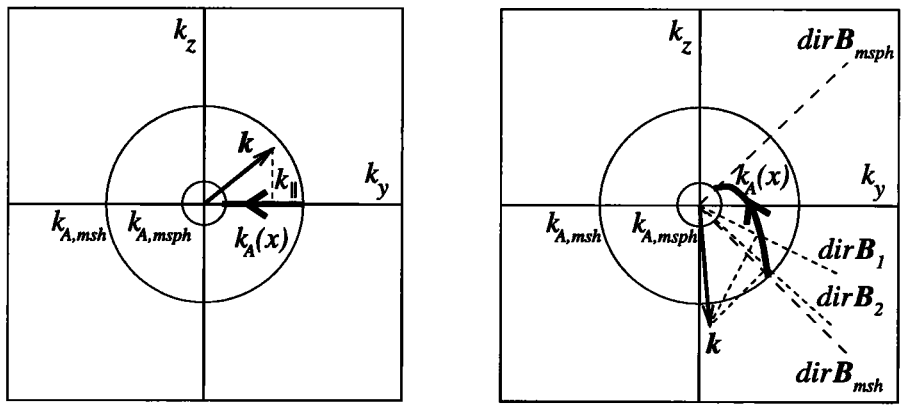

Figure 6. Hodogram of $k_A(x)$ in the k_y, k_z plane. The y axis is the bisector of $B^{(0)}_{\mathrm{msph}}$ and $B^{(0)}_{\mathrm{msh}}$, or, equivalently, of $k_{\mathrm{A,msph}}$ and $k_{\mathrm{A,msh}}$. The two circles indicate the projection of the wave number in the magnetosheath (large circle) and in the magnetosphere (small circle). The resonant condition is fulfilled at points where the projection of k on the direction of B equals $k_A(x)$. (a) Zero magnetic shear: the hodogram is a straight line segment, and at most one resonance point exists if $k_A(x)$ is monotonous. (b) High magnetic shear: for a given k, resonance with $|k_\parallel| = k_A(x)$ can occur at several points inside the magnetopause simultaneously (two resonances in this case).

tosheath and magnetospheric magnetosonic waves (rotated as determined by the 90° magnetic shear) and the resonance conditions. Figure 7b counts the number of resonance points. No resonant amplification can occur when $k_t < k_{A,\mathrm{msph}}$ (the circular region with class 1 solutions in the center of Figure 7a). When $k_{\parallel,\mathrm{msph}} > k_{A,\mathrm{msph}}$ with k_t not much larger than $k_{A,\mathrm{msph}}$, resonance occurs near the magnetospheric edge of the magnetopause. This is shown in Figure 7b by two straight lines running from the upper left to the lower right, which are tangent to a circle (not drawn) with radius $k_{A,\mathrm{msph}}$ and perpendicular to $k_{A,\mathrm{msph}}$, and which demarcate the region where resonance occurs. Resonance occurs near the magnetosheath edge of the magnetopause when $k_{\parallel,\mathrm{msh}} < k_{A,\mathrm{msh}}$ with k_t not much smaller than $k_{A,\mathrm{msh}}$, which translates into two demarcation lines running from the lower left to the upper right, which are tangent to a circle (not drawn) with radius $k_{A,\mathrm{msh}}$ and perpendicular to $k_{A,\mathrm{msh}}$. Again, a similar reasoning can be applied to the k_S hodogram (resonance condition (6)), leading to two additional pairs of straight lines that demarcate regions with additional resonance points.

4.3. Trapped Populations

We have shown that the occurrence of resonance is closely related to the k_A and k_S hodograms. However, the unperturbed magnetopause configuration used above was to some extent arbitrary. It is known that, at least for large magnetic shear configurations, the magnetic field strength often is de-

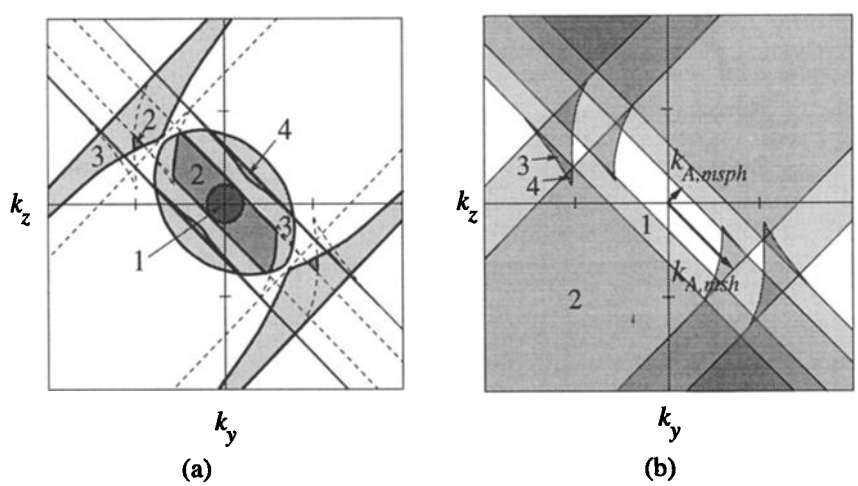

Figure 7. Propagation of waves at the magnetopause for 90° magnetic shear. The y axis is the bisector of $B^{(0)}_{\mathrm{msph}}$ and $B^{(0)}_{\mathrm{msh}}$. The magnetosonic propagation domains of Figure 2 are rotated over +45° and −45°. (a) Solution classes. (b) Number of resonance points.

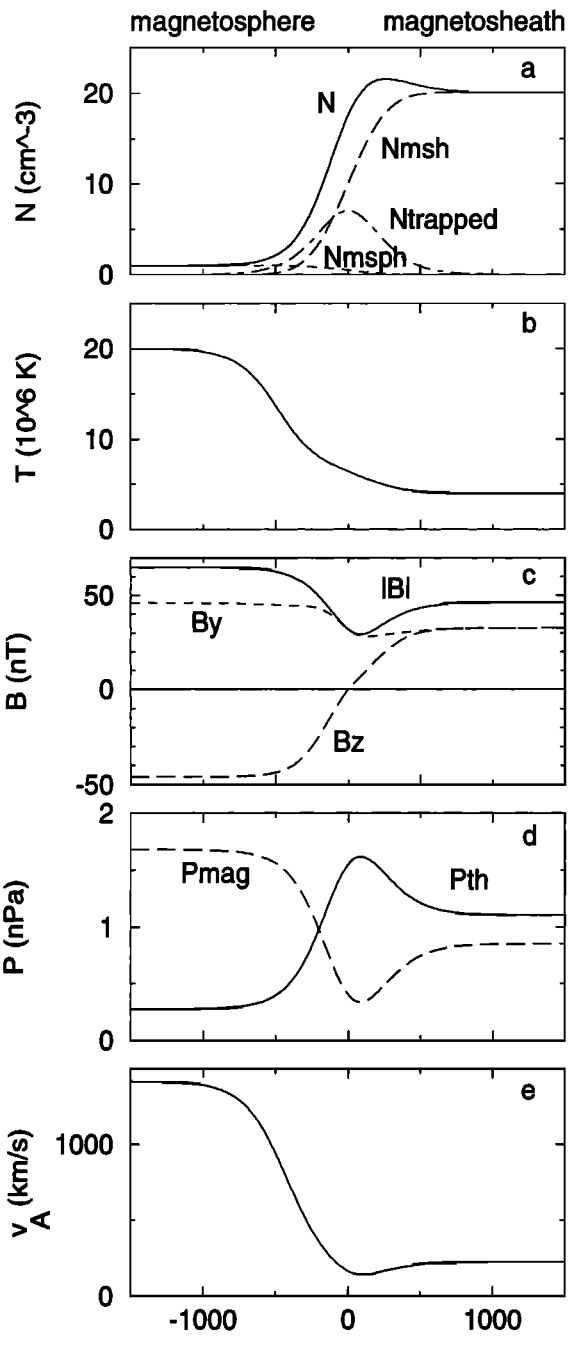

Figure 8. Magnetopause equilibrium when a trapped population is present (90° magnetic shear). (a) Magnetosheath, magnetospheric, trapped population, and total number density; (b) temperature; (c) magnetic field; (d) magnetic and thermal pressure; and (e) Alfvén velocity reaching a local minimum inside the magnetopause.

pressed inside the magnetopause layer because of the presence of "trapped" particles that carry the diamagnetic current inside the magnetopause layer [*Song et al.*, 1993; *Hubert et al.*, 1998]; $k_A(x)$ and $k_S(x)$ will then no longer be monotonous. It is therefore more realistic to add a plasma component with density profile [*Harris*, 1961]

$$\rho^{(0)}_{\text{trapped}}(x) = \rho^{*}_{\text{trapped}}/\cosh^2(x/D)$$

and temperature $T^{*}_{\text{trapped}} = (T^{*}_{\text{msph}} T^{*}_{\text{msh}})^{1/2}$, the geometric mean of the magnetosheath and magnetospheric temperatures. The structure of such a transition is illustrated by Figure 8 for the case of a 90° rotation, with $\rho^{*}_{\text{trapped}}/m = 7\ \text{cm}^{-3}$. Since $k_A(x)$ is no longer monotonous, resonant amplification can occur at more points (if $\theta(x)$ also is not monotonous, even more resonant points can exist). The diagrams showing the solution classes and the number of resonance points are given in Figure 9. Since including the trapped population decreases the Alfvén velocity, more resonant points exist near the center of the transition, with resonance for larger wave vectors; the corresponding waves are not always able to propagate through the magnetosheath. It is, however, possible that ULF perturbations become trapped in such Alfvén velocity valleys [*Zhu and Kivelson*, 1989].

5. Discussion and Conclusions

The purpose of the present paper was to re-examine the mechanism of resonant amplification of MHD waves at the magnetopause discussed by *Belmont et al.* [1995] in a more realistic subsolar magnetopause setting that includes the effects of plasma pressure, magnetic field rotation, and trapped populations. We have computed the spatial profiles of all possible types of wave solutions, their polarization, and the corresponding energy flux profiles.

The inclusion of thermal pressure effects leads to the apparition of slow-mode resonances in addition to Alfvén wave resonances. Indeed, there exist two types of mode conversion: fast-mode waves can couple to Alfvén or slow-mode waves. A first implication is that there exists a fourth wave solution class in addition to those distinguished by *Belmont et al.* [1995]. The four classes include waves propagating through the magnetopause, with or without resonant amplification, and evanescent waves with or without resonant amplification. A second implication is that for a given frequency, resonant amplification can occur at several points inside the magnetopause simultaneously. Even more resonance points appear when there is a significant rotation of the magnetic field across the magnetopause and when there are diamagnetic effects due to the presence of trapped particles that carry the magnetopause current.

The results reported here are based on a "closed" magnetosphere model. Indeed, we have adopted a tangential discontinuity magnetopause structure. It can also be shown (see the Appendix) that in the present model the mass flux across the magnetopause is zero (at least up to the second order). Nevertheless, our findings illustrate that there can be a significant transport of wave energy across a closed magnetosphere boundary. The calculations demonstrate that there are different possibilities for wave energy transport.

A first possibility is that the energy carried by an earthward propagating magnetosheath wave is transmitted across the magnetopause without appreciable attenuation if its frequency is below the magnetospheric Alfvén and slow-mode resonance frequencies. Conversely, for a given frequency, transmission occurs when the tangential wave vector is below the limit set by the magnetospheric Alfvén and slow-

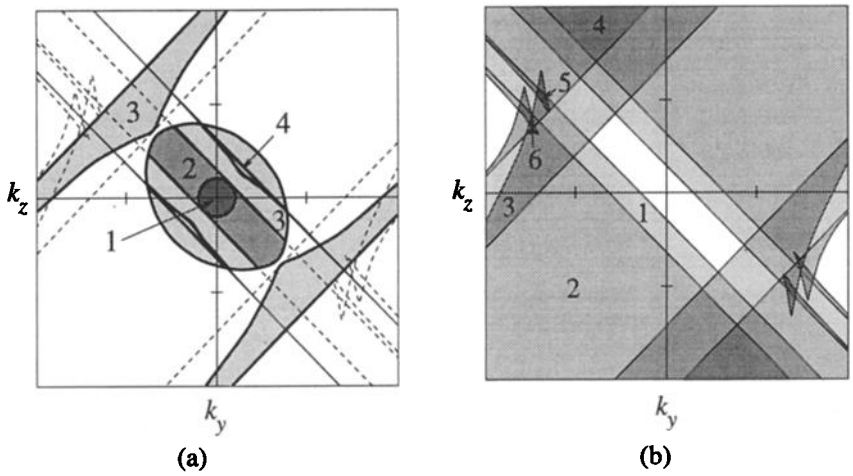

Figure 9. Propagation of waves at the magnetopause for 90° magnetic shear when a trapped population is present. The y axis is the bisector of $\boldsymbol{B}^{(0)}_{\mathrm{msph}}$ and $\boldsymbol{B}^{(0)}_{\mathrm{msh}}$. The magnetosonic propagation domains of Figure 2 are rotated over +45° and −45°. (a) Solution classes. (b) Number of resonance points.

mode speeds; the incident wavefronts then are nearly planar. An example of such waves are those in the milliHertz frequency range discussed by *Southwood* [1974]: these waves propagate across the magnetopause, but as the magnetic field and the Alfvén and slow-mode velocities increase upon approaching Earth, mode conversion eventually takes place on drift shells in the inner magnetosphere. This mechanism is believed to be the source of micropulsations. The wave energy is deposited inside the magnetosphere.

Second, if resonance occurs, mode conversion of the incident waves (which have a small frequency modulation in our model) results in diverting the normally incident energy flux into the tangential directions at the sites of resonance: the energy is carried away by surface waves, traveling parallel to the magnetic field. If we would have introduced a dissipation mechanism in our model, the effect would be that energy is fed to the plasma inside the magnetopause current layer. The mode conversion mechanism then could be the source of heating effects at the magnetopause. The present paper shows that mode conversion generally does not occur at a single point but that it can occur at many places inside the magnetopause layer simultaneously. This is even more so when the incident waves are not monochromatic. Wave energy deposition is therefore expected to take place throughout the entire magnetopause current layer.

Last, an incident wave can be reflected so that it delivers no energy to the magnetosphere.

The calculations presented here illustrate that all combinations of these three situations can occur. We find that most of the fast magnetosonic waves that propagate through the magnetosheath give rise to resonant amplification at the magnetopause, unless their frequency is sufficiently low so that they can penetrate into the inner magnetosphere, where mode conversion may still be their ultimate fate. Resonant amplification at the magnetopause appears to be the rule, rather than the exception. These findings seem to support the following picture: incident magnetosheath ULF waves (possibly generated near the bow shock) lead to enhanced fluctuation amplitudes at the magnetopause because of resonant amplification there, while the fluctuation level drops to relatively low values in the magnetosphere as a large fraction of the waves cannot propagate across the magnetopause. This is in qualitative agreement with observations. In terms of energy flux, this implies that a significant fraction of the incident flux is reflected, a significant fraction is absorbed at the magnetopause, and only a small fraction is able to reach the inner magnetosphere.

It is outside the scope of this paper to estimate the total wave energy flux deposited into the magnetopause current layer from a quantitative point of view because of the many simplifications that have been made in the analysis. Indeed, we have left the dissipation mechanism unspecified. The model is only one-dimensional. Also, the ideal MHD single-fluid hypothesis limits the generality of the results. The electron response to the ULF field is expected to be rather unimportant because of the low frequencies considered, justifying a single-fluid approach. Finite gyroradius effects and the accompanying charge separation electric fields, however, might be of some importance, as the magnetopause is often only a few ion gyroradii thick [*Berchem and Russell*, 1982]. First results in this field have been published by *Johnson and Cheng* [1997]. The present paper dealt with monochromatic waves with a frequency that is negligible with respect to the proton gyrofrequency (MHD conditions). In order to take into account the broadband spectrum observed in the magnetosheath, ion inertia effects should be included in the model. This might have some consequences on the behavior of the waves, since waves propagating in a homogeneous medium are modified by ion inertia effects [*Belmont and Rezeau*, 1987]. A linear perturbation analysis is useful for evaluating the effects of ULF fluctuations in the 0.1–1 Hz range on the subsolar magnetopause in the quasi-steady regime, at least

in a first approximation, but the observed fluctuation levels suggest that nonlinear effects can be important [*Rezeau et al.*, 1989].

Appendix: Linearized MHD Equations

The linearization of the ideal MHD equations has been discussed in the literature, for example, by *Walker* [1981]. This appendix describes the linearization procedure in the context of monochromatic waves at the one-dimensional subsolar magnetopause, and adds a discussion of the computation of the energy flux.

Let x be the outward normal to the (planar) magnetopause. Denoting the mass density by ρ, the bulk velocity by $\boldsymbol{v}$, the magnetic and electric fields by $\boldsymbol{B}$ and $\boldsymbol{E}$, the thermal pressure by p, the energy by $\mathcal{E}$, and the ion temperature by T, the one-dimensional single-fluid ideal MHD equations are

$$\frac{\partial \rho}{\partial t} + \nabla\cdot(\rho \boldsymbol{v}) = 0, \quad \text{(A1)}$$

$$\frac{\partial \rho \boldsymbol{v}}{\partial t} + \nabla\cdot[\rho \boldsymbol{v}\boldsymbol{v} + (p + \frac{B^2}{2\mu_0})\boldsymbol{I} - \frac{1}{\mu_0}\boldsymbol{B}\boldsymbol{B}] = \boldsymbol{0}, \quad \text{(A2)}$$

$$\frac{\partial \boldsymbol{B}}{\partial t} + \nabla\times\boldsymbol{E} = \boldsymbol{0}, \quad \text{(A3)}$$

$$\frac{\partial \mathcal{E}}{\partial t} + \nabla\cdot[(\frac{\rho v^2}{2} + \frac{\gamma p}{\gamma - 1})\boldsymbol{v} + \frac{1}{\mu_0}\boldsymbol{E}\times\boldsymbol{B}] = 0, \quad \text{(A4)}$$

supplemented by

$$\begin{aligned} \nabla\cdot\boldsymbol{B} &= 0, \\ \mathcal{E} &= \frac{\rho v^2}{2} + \frac{B^2}{2\mu_0} + \frac{p}{\gamma - 1}, \\ \boldsymbol{E} &= -\boldsymbol{v}\times\boldsymbol{B}, \\ p &= k_B \rho T/m, \end{aligned}$$

where k_B is Boltzmann's constant, m the ion mass, and γ the adiabatic exponent of the plasma ($\gamma = 5/3$). The Lagrangian displacement $\boldsymbol{\xi}$ of a fluid element is related to the velocity by

$$\boldsymbol{v} = \frac{d\boldsymbol{\xi}}{dt} = \frac{\partial \boldsymbol{\xi}}{\partial t} + (\boldsymbol{v}\cdot\nabla)\boldsymbol{\xi}.$$

We consider first-order perturbed quantities of the form $q(\boldsymbol{r}, t) \approx q^{(0)}(x) + q^{(1)}(x)$. Moreover, we limit the discussion to monochromatic perturbations $q^{(1)} = \hat{q}^{(1)} e^{i(\boldsymbol{k}_t\cdot\boldsymbol{r} - \omega t)}$, where $\boldsymbol{r} = [x, y, z]$ is the position vector of a plasma element, $\nu = \omega/2\pi$ the frequency of the perturbation, and $\boldsymbol{k}_t = [0, k_y, k_z]$ the tangential wave vector. We consider the static case $\boldsymbol{v}^{(0)} \equiv \boldsymbol{0}$. Introducing the operator $\hat{\nabla} = [\partial/\partial x, ik_y, ik_z]$, the linearized equations can be written in terms of the normal displacement $\hat{\xi}_x$ and the normal pressure perturbation $\hat{\tau}$:

$$\begin{aligned} -i\omega\hat{\rho}^{(1)} + (\hat{\nabla}\cdot\hat{\boldsymbol{v}}^{(1)} + \hat{\boldsymbol{v}}^{(1)}\cdot\nabla)\rho^{(0)} &= 0, \\ -i\omega\rho^{(0)}\hat{\boldsymbol{v}}^{(1)} + \hat{\nabla}\hat{\tau} & \\ -\frac{1}{\mu_0}[(\hat{\boldsymbol{B}}^{(1)}\cdot\nabla)\boldsymbol{B}^{(0)} + i(\boldsymbol{k}\cdot\boldsymbol{B}^{(0)})\hat{\boldsymbol{B}}^{(1)}] &= \boldsymbol{0}, \\ -i\omega\hat{\boldsymbol{B}}^{(1)} - i(\boldsymbol{k}\cdot\boldsymbol{B}^{(0)})\hat{\boldsymbol{v}}^{(1)} + (\hat{\nabla}\cdot\hat{\boldsymbol{v}}^{(1)} + \hat{\boldsymbol{v}}^{(1)}\cdot\nabla)\boldsymbol{B}^{(0)} &= \boldsymbol{0}, \\ -i\omega(\hat{p}^{(1)} - c_s^2\hat{\rho}^{(1)}) + \hat{v}_x^{(1)}(\frac{\partial p^{(0)}}{\partial x} - c_s^2\frac{\partial \rho^{(0)}}{\partial x}) &= 0, \\ i\omega\hat{\boldsymbol{\xi}} + \hat{\boldsymbol{v}}^{(1)} &= \boldsymbol{0}, \\ -\hat{\tau} + \hat{p}^{(1)} + \frac{1}{\mu_0}\boldsymbol{B}^{(0)}\cdot\hat{\boldsymbol{B}}^{(1)} &= 0, \end{aligned}$$

where $c_s = \sqrt{\gamma p^{(0)}/\rho^{(0)}}$ is the local sound speed in the unperturbed configuration. The first four equations are the transformed versions of (A1)–(A4), while the latter two correspond to the definitions of $\hat{\boldsymbol{\xi}}$ and $\hat{\tau}$. With some algebra one can express all perturbed quantities as functions of $\hat{\xi}_x$ and $\hat{\tau}$, reducing the system to the two coupled equations [*Belmont et al.*, 1995]:

$$\frac{1}{iK_x}\frac{\partial \hat{\tau}}{\partial x} = G\hat{\xi}_x, \quad \text{(A5)}$$

$$\frac{1}{iK_x}\frac{\partial \hat{\xi}_x}{\partial x} = \frac{1}{G}\hat{\tau}, \quad \text{(A6)}$$

for $\hat{\xi}_x$ and $\hat{\tau}$ (or, equivalently, one obtains a single equation for $g = \hat{\tau}/\hat{\xi}_x$, as discussed in the paper). Defining $u^2 = v_A^2 + c_s^2\Omega^2/\omega^2$, one then finds

$$\hat{\xi}_{yz} = \frac{i}{\omega^2 - k_t^2 u^2}(\frac{\boldsymbol{k}\cdot\boldsymbol{B}^{(0)}}{\mu_0\rho^{(0)}}B_{yz}^{(0)} - u^2 k_{yz})\frac{\partial \hat{\xi}_x}{\partial x}. \quad \text{(A7)}$$

The perturbed solution components are obtained from $\hat{\boldsymbol{\xi}}$ by

$$\hat{\rho}^{(1)} = -\hat{\boldsymbol{\xi}}\cdot\nabla\rho^{(0)} - \rho^{(0)}\hat{\nabla}\cdot\hat{\boldsymbol{\xi}}, \quad \text{(A8)}$$

$$\hat{\boldsymbol{v}}^{(1)} = -i\omega\hat{\boldsymbol{\xi}}, \quad \text{(A9)}$$

$$\hat{\boldsymbol{B}}^{(1)} = i(\boldsymbol{k}\cdot\boldsymbol{B}^{(0)})\hat{\boldsymbol{\xi}} - (\hat{\nabla}\cdot\hat{\boldsymbol{\xi}})\boldsymbol{B}^{(0)} - (\hat{\boldsymbol{\xi}}\cdot\nabla)\boldsymbol{B}^{(0)}, \quad \text{(A10)}$$

$$\hat{p}^{(1)} = -\hat{\boldsymbol{\xi}}\cdot\nabla p^{(0)} - \gamma p^{(0)}\hat{\nabla}\cdot\hat{\boldsymbol{\xi}}, \quad \text{(A11)}$$

and the electric field is

$$\hat{\boldsymbol{E}}^{(1)} = -\hat{\boldsymbol{v}}^{(1)}\times\hat{\boldsymbol{B}}^{(0)}. \quad \text{(A12)}$$

The mass flux is $\boldsymbol{\psi} = \rho\boldsymbol{v}$. The flux ψ_x gives the mass transport across the magnetopause. In the static case, $\psi_x^{(0)} \equiv 0$ and

$$\begin{aligned} \psi_x^{(1)} &= \rho^{(0)} v_x^{(1)}, \\ \psi_x^{(2)} &= \rho^{(1)} v_x^{(1)} + \rho^{(0)} v_x^{(2)}, \end{aligned}$$

where $v_x^{(2)} = (\nabla\cdot\boldsymbol{\xi})v_x^{(1)}$. The time-averaged mass flux is $\bar{\psi}_x = \bar{\psi}_x^{(2)}$ (since $\bar{\psi}_x^{(1)} \equiv 0$). Denoting the complex conjugate by a star, one obtains

$$\begin{aligned} \bar{\psi}_x &= \frac{1}{2}\mathrm{Re}\{-\hat{\boldsymbol{\xi}}\cdot\nabla\rho^{(0)}\} \\ &= -\frac{\omega}{2}\nabla\rho^{(0)}\mathrm{Re}\{i\hat{\boldsymbol{\xi}}\cdot\boldsymbol{\xi}^*\} = 0. \end{aligned} \quad \text{(A13)}$$

The energy flux is (see (A4))

$$\boldsymbol{\phi} = (\frac{\rho v^2}{2} + \frac{\gamma p}{\gamma - 1})\boldsymbol{v} + \frac{1}{\mu_0}\boldsymbol{E}\times\boldsymbol{B},$$

where the first term is the flux of kinetic energy and the second term the Poynting flux of electromagnetic energy. The flux ϕ_x characterizes the transfer of energy from the magnetosheath to the magnetosphere. In the static case, $\phi_x^{(0)} \equiv 0$

and

$$\phi_x^{(1)} = (\frac{\gamma}{\gamma-1}p^{(0)} + \frac{1}{\mu_0}B^{(0)2})v_x^{(1)},$$

$$\phi_x^{(2)} = \frac{\gamma}{\gamma-1}(p^{(0)}v_x^{(2)} + p^{(1)}v_x^{(1)}) + \frac{1}{\mu_0}(2\boldsymbol{B}^{(0)}\cdot\boldsymbol{B}^{(1)}v_x^{(1)} - \boldsymbol{B}^{(0)}\cdot\boldsymbol{v}^{(1)}B_x^{(1)} + B^{(0)2}v_x^{(2)}),$$

where $B_x^{(1)} = -(\boldsymbol{k}\cdot\boldsymbol{B}^{(0)}/\omega)v_x^{(1)}$. The time-averaged energy flux $\bar{\phi}_x = \bar{\phi}_x^{(2)}$ (since $\bar{\phi}_x^{(1)} \equiv 0$) is obtained as

$$\bar{\phi}_x = \frac{1}{2}\mathrm{Re}\{[\frac{\gamma}{\gamma-1}(p^{(0)}\hat{\boldsymbol{\nabla}}\cdot\hat{\boldsymbol{\xi}} + \hat{p}^{(1)}) + \frac{1}{\mu_0}(2\boldsymbol{B}^{(0)}\cdot\hat{\boldsymbol{B}}^{(1)} + \frac{\boldsymbol{k}\cdot\boldsymbol{B}^{(0)}}{\omega}\boldsymbol{B}^{(0)}\cdot\hat{\boldsymbol{v}}^{(1)} + B^{(0)2}\hat{\boldsymbol{\nabla}}\cdot\hat{\boldsymbol{\xi}})]\,\hat{v}_x^{(1)*}\}. \quad \text{(A14)}$$

Let us finally check that (A14) does lead to a constant energy flux when k_t is real. Using (A7)–(A11), the flux can be expressed as a function of $\hat{\xi}_x$ only:

$$\bar{\phi}_x = \frac{\omega\rho^{(0)}\Omega^2u^2}{2(\omega^2 - k_t^2u^2)}I,$$

with

$$I = \mathrm{Im}\{\frac{\partial\hat{\xi}_x}{\partial x}\hat{\xi}_x^*\}.$$

From (A5)–(A6) it immediately follows that

$$\frac{\partial}{\partial x}\left(\frac{G}{iK_x}\frac{\partial\hat{\xi}_x}{\partial x}\right) = iK_xG\hat{\xi}_x.$$

Multiplying with $\hat{\xi}_x^*$ and considering only the imaginary part, we find

$$\frac{1}{I}\frac{\partial I}{\partial x} = -\frac{iK_x}{G}\frac{\partial}{\partial x}\left(\frac{G}{iK_x}\right),$$

and hence

$$I = \frac{iK_x\kappa}{G} = \frac{K_x^2\kappa}{\rho^{(0)}\Omega^2},$$

where the integration constant κ is real. The energy flux finally turns out to be

$$\bar{\phi}_x = \frac{\omega\kappa}{2},$$

that is, it remains constant in regular points of the differential problem.

Acknowledgments. Work by J.D.K. and M.R. was performed at the Belgian Institute for Space Aeronomy, partially under a PRODEX contract with ESA. J.D.K. and M.R. acknowledge the support of the Belgian Federal Services for Scientific, Technical and Cultural Affairs.

Michel Blanc thanks Rudolf Treumann and another referee for their assistance in evaluating this paper.

References

Belmont, G., and L. Rezeau, Finite Larmor radius effects: The two-fluid approach, *Ann. Geophys., 5A*, 59–70, 1987.

Belmont, G., F. Reberac, and L. Rezeau, Resonant amplification of magnetosheath MHD fluctuations at the magnetopause, *Geophys. Res. Lett., 22*, 295–298, 1995.

Berchem, J., and C. T. Russell, The thickness of the magnetopause current layer: ISEE 1 and 2 observations, *J. Geophys. Res., 87*, 2108–2114, 1982.

De Keyser, J., and M. Roth, Equilibrium conditions for the tangential discontinuity magnetopause, *J. Geophys. Res., 102*, 9513–9530, 1997.

Engebretson, M. J., N. Lin, W. Baumjohann, H. Lühr, B. J. Anderson, L.J. Zanetti, T.A. Potemra, R.L. McPherron, and M.G. Kivelson, A comparison of ULF fluctuations in the solar wind, magnetosheath, and dayside magnetosphere, 1, Magnetosheath morphology, *J. Geophys. Res., 96*, 3441–3454, 1991.

Harris, E. G., On a plasma sheath separating regions of oppositely directed magnetic fields, *Nuovo Cimento, 23*, 115, 1961.

Hollweg, J. V., A simple mechanical model for resonance absorption: The Alfvén resonance, *J. Geophys. Res., 102*, 24,127–24,137, 1997.

Hubert, D., C. C. Harvey, M. Roth, and J. De Keyser, Electron density at the subsolar magnetopause for high magnetic shear: ISEE 1 and 2 observations, *J. Geophys. Res.*, 103, 6685–6692, 1998.

Johnson, J. R., and C. Z. Cheng, Kinetic Alfvén waves and plasma transport at the magnetopause, *Geophys. Res. Lett., 24*, 1423–1426, 1997.

LaBelle, J., and R. A. Treumann, Plasma waves at the dayside magnetopause, *Space Sci. Rev., 47*, 175–202, 1988.

Lee, L. C., and J. R. Kan, A unified kinetic model of the tangential magnetopause structure, *J. Geophys. Res., 84*, 6417–6426, 1979.

Paschmann, G., B. U. Ö. Sonnerup, I. Papamastorakis, N. Sckopke, G. Haerendel, S. J. Bame, J. R. Asbridge, J. T. Gosling, C. T. Russell, and R. C. Elphic, Plasma acceleration at the Earth's magnetopause: Evidence for reconnection, *Nature, 282*, 243–246, 1979.

Rezeau, L., A. Morane, S. Perraut, A. Roux, and R. Schmidt, Characterization of Alfvénic fluctuations in the magnetopause boundary layer, *J. Geophys. Res., 94*, 101–110, 1989.

Rezeau, L., A. Roux, and C. T. Russell, Characterization of small-scale structures at the magnetopause from ISEE measurements, *J. Geophys. Res., 98*, 179–186, 1993.

Roth, M., J. De Keyser, and M. M. Kuznetsova, Vlasov theory of the equilibrium structure of tangential discontinuities in space plasmas, *Space Sci. Rev., 76*, 251–317, 1996.

Song, P., C. T. Russell, and C. Y. Huang, Wave properties near the subsolar magnetopause: Pc 1 waves in the sheath transition layer, *J. Geophys. Res., 98*, 5907–5923, 1993.

Southwood, D. J., Some features of field line resonances in the magnetosphere, *Planet. Space Sci., 22*, 483–491, 1974.

Su, S.-Y., and B. U. Ö. Sonnerup, First-order orbit theory of the rotational discontinuity, *Phys. Fluids, 11*, 851–857, 1968.

Walker, A. D. M., The Kelvin-Helmholtz instability in the low-latitude boundary layer, *Planet. Space Sci., 29*, 1119–1133, 1981.

Zhu, X., and M. G. Kivelson, Global mode ULF pulsations in a magnetosphere with a nonmonotonic Alfvén velocity profile, *J. Geophys. Res., 94*, 1479–1485, 1989.

G. Belmont, F. Reberac, and L. Rezeau, Centre d'Étude des Environnements Terrestre et Planétaires, 10/12 Avenue de l'Europe, 78140 Vélizy, France. (Gerard.Belmont@cetp.ipsl.fr; Fabien.Reberac@cetp.ipsl.fr; Laurence.Rezeau@cetp.ipsl.fr)

J. De Keyser and M. Roth, Belgian Institute for Space Aeronomy, Ringlaan 3, B-1180 Brussels, Belgium. (Johan.DeKeyser@oma.be; Michel.Roth@oma.be)

(Received April 15, 1998; revised September 23, 1998; accepted September 28, 1998.)